THE JOURNAL OF BIOLOGICAL CHEMISTRY VOL. 283, NO. 15, pp. 9651–9658, April 11, 2008

Solute Carrier 11 Cation Symport Requires Distinct Residues in Transmembrane Helices 1 and 6*[S]

Received for publication, December 4, 2007, and in revised form, January 18, 2008 Published, JBC Papers in Press, January 28, 2008, DOI 10.1074/jbc.M709906200

Pascal Courville[‡], Eva Urbankova[§], Christopher Rensing[¶], Roman Chaloupka[§], Matthias Quick[‖], and Mathieu F. M. Cellier[‡1]

From the [‡]INRS-Institut Armand-Frappier, 531 Bd des prairies, Laval, Québec H7V 1B7, Canada, the [§]Faculty of Mathematics and Physics, Charles University, Institute of Physics, Ke Karlovu 5, 121 16 Prague 2, Czech Republic, the [¶]Department of Soil, Water, and Environmental Science, University of Arizona, Tucson, Arizona 85721, and the [‖]Center for Molecular Recognition, Columbia University, College of Physicians and Surgeons 11-401, New York, New York 10032

Ubiquitous solute carriers 11 (SLC11) contribute to metal-ion homeostasis by importing Me^{2+} and H^+ into the cytoplasm. To identify residues mediating cation symport, *Escherichia coli* proton-dependent manganese transporter (MntH) was mutated at five SLC11-specific transmembrane (TM) sites; each mutant activity was compared with wild-type MntH, and the biochemical results were tested by homology threading. Cd^{2+} and H^+ uptake kinetics were analyzed in whole cells as a function of pH and temperature, and right-side out membrane vesicles were used to detail energy requirements and to probe site accessibility by Cys replacement and thiol modification. This approach revealed that TM segment 1 (TMS1) residue Asp^{34} couples H^+ and Me^{2+} symport and contributes to MntH forward transport electrogenicity, whereas the TMS6 His^{211} residue mediates pH-dependent Me^{2+} uptake; MntH Asn^{37}, Asn^{250}, and Asn^{401} in TMS1, TMS7, and TMS11 participate in transporter cycling and/or helix packing interactions. These biochemical results fit the LeuT/SLC6 structural fold, which suggests that conserved peptide motifs Asp^{34}-Pro-Gly (TMS1) and Met-Pro-His^{211} (TMS6) form antiparallel "TM helix/extended peptide" boundaries, lining a "pore" cavity and enabling H^+-dependent Me^{2+} import.

Members of the natural resistance-associated macrophage protein (Nramp/SLC11) family (1, 2) are structurally conserved transporters catalyzing cellular uptake of redox metals such as Fe^{2+} and Mn^{2+}. Mutations of *NRAMP1* orthologs in terrestrial vertebrates were linked to host phagocyte innate response to infections and immune diseases (3, 4). Genetic defects in *NRAMP2* (aka *DMT1*) affect iron homeostasis (intestinal absorption, erythropoiesis, and tissue distribution (2, 5, 6). Despite their medical importance, insight into the structure and function of SLC11 transporters is largely missing. Elucidation of the molecular mechanism underlying electrogenic H^+ and Me^{2+} symport represents a milestone in the pursuit of future therapeutic approaches to treat Me^{2+} homeostasis disorders, including brain diseases (7).

Prokaryotic orthologs of essential eukaryotic membrane transport functions represent attractive models to advance understanding of the mechanism of transport (8, 9). Studies from different groups showed that *Escherichia coli* proton-dependent manganese transporter (MntH)[2] is a valuable system for structure/function studies of H^+ and Me^{2+} symport (10–13). MntH TM topology was established and selected mutations resulted in similar phenotypes in MntH and Nramp2 variants (6, 14, 15). In addition, *E. coli* MntH wild-type (WT) lacks cysteine residues, and site-directed introduction of Cys moieties combined to thiol modifications allows for detailed structural and functional mapping (16).

SLC11-dependent transport is typified by broad selectivity (*e.g.* Mn^{2+}, Cd^{2+}, Fe^{2+}, Co^{2+}, and Ni^{2+}) and Me^{2+}-specific interactions, including a range of Me^{2+}/H^+ stoichiometries depending on external conditions (10, 17–19). The H^+-dependent Me^{2+} transport mechanism of eukaryotic Nramp homologs was deduced from studies of Me^{2+} uptake and Me^{2+}-evoked currents, the external pH altering the transporter affinity for Me^{2+} and the stoichiometry of H^+ and Me^{2+} fluxes (2, 5). Kinetic models for H^+-coupled transport usually imply that H^+ binding or uptake depends at least partly on the membrane potential ($\Delta\psi$, and at high proton concentration (pH 5.5), large Me^{2+}-induced currents are mainly due to H^+ charge transfer across the membrane (17, 19).

To identify features defining the mechanism of transport of the SLC11 family, sites representing evolutionary type II rate shifts were targeted because they represent a radical shift in amino acid properties, which can contribute to functional divergence among homologous proteins including membrane proteins (20–22). Phylogenetic analyses distinguished the SLC11 family from a group of distantly related sequences (out-

* This work was supported in part by Canadian Institutes of Health Research Grant MOP-78014-MI (to M. C.), Czech Science Foundation Grant 204/07/0558 (to R. C.), and the Fondation Armand-Frappier (to P. C.). The costs of publication of this article were defrayed in part by the payment of page charges. This article must therefore be hereby marked "*advertisement*" in accordance with 18 U.S.C. Section 1734 solely to indicate this fact.

[S] The on-line version of this article (available at http://www.jbc.org) contains supplemental Figs. S1–S5, Table S1, and supplemental Methods 1 and 2.

[1] To whom correspondence should be addressed: INRS-Institut Armand-Frappier, 531, Bd des prairies, Laval, QC H7V 1B7, Canada. Fax: 450-686-5301; E-mail: mathieu.cellier@iaf.inrs.ca.

[2] The abbreviations used are: MntH, proton-dependent manganese transporter; F5M, fluorescein 5-maleimide; NEM, *N*-ethylmaleimide; RSOV, right-side out vesicles; ISOV, inside out vesicles; PMS, methylphenazonium methyl sulfate; Asc, ascorbate; CCCP, carbonyl cyanide *m*-chlorophenylhydrazone; Nramp, natural resistance-associated macrophage protein; SLC11, solute carrier 11; SLC6, solute carrier 6; TMS, transmembrane segment; LeuT, leucine transporter; EmrD, multidrug transporter EmrD; $\Delta\psi$, membrane potential; WT, wild type; Mes, 4-morpholineethanesulfonic acid; Pipes, 1,4-piperazinediethanesulfonic acid.

group <30% amino acid identity). Four type II rate shifts were identified at TM sites displaying polar or charged SLC11-specific amino acids matched by distinct outgroup-specific residues (10). Reciprocal residue exchange and additional mutations at each of these sites in TMS1, TMS6, and TMS11 were characterized, showing individual roles of each site in the Me^{2+} and/or H^+ symport (10); among them residue Asp^{34} appeared crucial for transport activity but its functional role remains undefined (10, 11).

The objective of this study was to elucidate the individual roles of the TM residues identified as evolutionary type II rate shift sites by analyzing the impact of the SLC11/outgroup reciprocal mutations on Me^{2+} and H^+ uptake kinetics and thermodynamics *in vivo* and *in vitro*, by probing the *in situ* accessibility of targeted sites, and by selecting a tridimensional structural fold obtained by threading that fits our experimental results.

EXPERIMENTAL PROCEDURES

Site-directed Mutagenesis of E. coli MntH—Site-directed mutagenesis was carried out as described previously (10). The oligonucleotide primers used to generate novel mutants are listed in supplemental Table 1. Mutant clones were selected by profiling *in vivo* Me^{2+} sensitivity conferred upon expression in a metallo-dependent *E. coli* background (12). Full-length DNA sequence was determined for one clone of several that were functionally tested (CEQ 2000XL, Beckman Coulter, Mississauga, ON). The 12TMS-His_{10} construct was generated by adding the 12th TMS of the *Lactobacillus casei* MntH Cβ1 homolog (23) and a His_{10} tag. A StuI restriction site was introduced prior to the *mntH* stop codon to enable swapping of a StuI-XbaI flanked fragment of *mntH Cβ1* (residues 469–530, followed by a poly-His coding sequence).

Fluorescent Measurements of H^+ Transport in Vivo—Metal-induced intracellular acidification was measured using a pH-dependent ratiometric green fluorescent protein, pHluorin, and cells resuspended at an A_{600} of 0.2 in 50 mM citrate-phosphate buffer (pH 4.7–5.7) (14). Fluorescence emission (wavelength 520 nm) was measured on a Fluoromax-2 spectrophotometer (Jobin-Yvon, SPEX) after dual excitation at 410 and 470 nm. MntH-dependent intracellular acidification was deduced from $[H^+]$ changes post-metal addition and monitored for 1000 s. Energy of activation (E_a) values were deduced from $[H^+]$ changes 250 s after addition of 10 μM Cd^{2+} at temperatures varying from 15 to 37 °C.

Preparation of Right-side Out and Inside Out Membrane Vesicles—*E. coli* strain G536 (24) lacking several Fe^{2+} and Mn^{2+} transport systems (W3110 Δ*fecABCDE*::*kan* Δ*zupT*::*cat* Δ*mntH* Δ*entC* Δ*feoABC*) was transformed with derivatives of pBAD24 expressing native or mutant MntH. Individual clones were cultured in LB medium containing ampicillin (100 μg/ml) at 37 °C and 250 rpm until an A_{600} of 0.6 was reached. MntH expression was induced for 1 h using 0.1% arabinose. Right-side out vesicles (RSOV) were prepared by osmotic lysis (25), except that spheroplasts were lysed in 0.1 M potassium P_i, pH 7.5, washed, and resuspended in 0.1 M Pipes-Mes, pH 7.5. Inside out vesicles (ISOV) were prepared by one passage of the cells (2.5 mg wet weight/ml) through an Aminco French Press at 16,000 p.s.i. in 0.1 M potassium P_i, pH 7.5, buffer (26). RSOV and ISOV were resuspended in 0.1 M Pipes-Mes, pH 7.5, at a concentration of 10–15 mg of protein/ml. The polarity of these preparations was tested by fluorescence spectrophotometry (supplemental Fig. S3) using indicators of (i) changes in $\Delta\psi$ or ΔpH resulting from respiration (negative/alkaline or positive/acidic inside, respectively, for RSOV or ISOV), or (ii) topological accessibility of single Cys residues introduced in MntH extramembranous loops formerly assigned to either side of the membrane (14). These Cys mutants (MntH 12TMS-His_{10}) catalyzed Cd^{2+}-induced intracellular H^+ uptake (supplemental Fig. 3, *E* and *F*).

$^{109}Cd^{2+}$ Transport Assays—We used Cd^{2+} as substrate for MntH because it triggers larger intracellular acidification compared with Mn^{2+}, Fe^{2+}, and Co^{2+} (10). ^{109}Cd (specific activity 60 mCi/μmol; GE Healthcare, Baie d'Urfé, Quebec, Canada) uptake was performed by a quick filtration assay in 0.1 (vesicles preparations) or 0.05 M Pipes-Mes (intact cells), pH 6.5 or 7.5, at 24 °C unless otherwise specified. Samples (0.1 ml) were removed at the indicated times and immediately filtered through 0.45-μm Metricel GN-6 filters (PALL, East Hills, NY; whole cells), 0.75-μm borosilicate GF75 microfiber filters (Advantec MFS Inc., Dublin, CA; RSOV), and 0.22-μm nitrocellulose filters (Whatman, Florham Park, NJ; ISOV). Filters were washed with 5 ml of ice-cold uptake buffer containing 1 mM $CdCl_2$. All experiments were performed at least in triplicate, using protein concentrations of 50 (RSOV), 200 (ISOV), and ~700 μg/ml (whole cells, corresponding to an OD_{420} of 10) as determined by protein assay using a modified Lowry procedure (27). Vesicles were energized by adding 2 mM L-ascorbate and 0.02 mM *N*-methylphenazonium methyl sulfate (PMS/Asc), 10 mM D-lactate, or 5 mM NADH, for 3.5 min prior to the addition of Cd^{2+}. Ionophores (1 μM valinomycin, 0.1 μM nigericin, and 10 μM carbonyl cyanide *m*-chlorophenylhydrazone, CCCP) were added 1 min prior to PMS/Asc addition. E_a (28) was measured using whole cells at pH 6.5 during the initial, linear phase of Cd^{2+} uptake (after 10 s or 1 min) at temperatures varying from 24 to 37 °C. MntH specificity for Mn^{2+} was verified using varying concentrations of Mn^{2+} to compete Cd^{2+} uptake. By fitting data to the Cheng-Prusoff equation, an apparent inhibitory constant, $K^i_{Mn} = 1.2 \pm 0.2$ μM at pH 6.5, and $[S] \sim K^{0.5}_{Cd} = 2.6 \pm 0.5$ μM Cd^{2+}, was obtained (29) (supplemental Fig. 1*A*), consistent with previous studies using $^{54}Mn^{2+}$ (13).

Fluorescence Measurements of Membrane Potential ($\Delta\psi$) in RSOV and ISOV—Fluorescent probes, 3,3′-dipropylthiadicarbocyanine iodide (1 μM) and bis-(1,3-dibutylbarbituric acid) pentamethine oxonol (1 μM), were used to monitor $\Delta\psi$ changes in energized vesicles as described (30). Fluorescence excitation and emission wavelengths were, respectively, 622 and 670 nm for 3,3′-dipropylthiadicarbocyanine iodide, and 588 and 614 nm for bis-(1,3-dibutylbarbituric acid)pentamethine oxonol. Measurements were performed either in 100 mM Pipes-Mes, 100 mM KCl, pH 7.5 (and 10 mM $CaCl_2$ or $MgSO_4$ in some cases), or 100 mM potassium P_i, 5 mM $MgSO_4$, pH 7.5. MntH electrogenicity was evaluated using RSOV (50 μg/ml proteins) energized with PMS/Asc (2/0.02 mM) and in the presence of 0.1 μM nigericin. Fluorescence changes indicating relative mem-

brane depolarization were recorded for 5 min post-addition of Cd^{2+}. 0.1 μM valinomycin was added finally as internal control.

Site-directed Thiol Fluorescence Labeling—Each MntH 12TMS-His_{10} Cys derivative conferred *in vivo* Me^{2+} sensitivity (supplemental Fig. 4*B*), consistent with respective data from prior mutagenesis (supplemental Fig. 2) (10), implying that Cys accessibility will reflect the functional structure of native MntH. RSOV (0.5 mg of protein) were labeled by incubation with 0.1 mM fluorescein 5-maleimide (F5M, Vector Laboratories, Burlingame, CA) at 23 °C for 10 min, prior to or after solubilization in detergent. When indicated RSOV were pretreated for 10 min with 0.5 mM 4-acetomido-4′-maleimidylstilbene 2,2′-disulfonic acid, disodium salt (Molecular Probes, Eugene, OR), or 0.5 mM *N*-ethylmaleimide (NEM) and then washed and resuspended or solubilized before labeling with F5M. ISOV (0.5 mg of proteins) were incubated for 5 min in the presence of 2.5 μM F5M; labeling was stopped by a 15-min incubation in 20 mM NEM. Membranes were solubilized, and the constructs purified as described under supplemental methods before SDS-PAGE (31) and Coomassie or silver nitrate staining (32). Prior to gel staining, F5M fluorescence was measured under a UV lamp equipped with a green filter using an Alpha Imager 3400 (Innotech, San Leandro, CA).

Western Blot Analyses—C-terminal tagged (-c-Myc or -12TMS-His_{10}) MntH variants were immunodetected in membrane preparations or in purified form as described (10) using anti-c-Myc (PerkinElmer Life Sciences) or anti-His (GE Healthcare) monoclonal antibodies.

Homology Modeling—Several approaches that use an alignment to map residues in a query sequence to sites in candidate template crystals structures were tested using the parameters specified by the developers, including Modeler (33), mGenThreader (34), and several others that are proposed on the meta-server LOMETS, including I-TASSER (9, 33, 35). Four sequences representative of the SLC11 family (two prokaryotic MntH and two eukaryotic Nramp) were tested and the results compiled to produce a consensus prediction. The PDB coordinates calculated were used visualize three-dimensional models using the freeware viewer PyMol (60). The root mean square deviation and *Z*-score of the LeuT models were verified using Combinatorial Extension (36), DaliLite (37), and MArkovian TRAnsition of Structure evolution (38).

RESULTS

Targeting Five Type II Evolutionary Rate Sites to Study the Mechanism of Me^{2+} and H^+ Symport—The functional impact of mutating four SLC11-specific TM sites (MntH Asp^{34}, Asn^{37}, His^{211}, and Asn^{401}; Ref. 10) suggested that further kinetic and thermodynamic analyses of mutants at these sites would inform understanding of structure-function relationships. We thus studied mutants in which the SLC11 residues were exchanged for the matching outgroup moiety. The presence of two Asn residues at selected sites suggested also include MntH TMS7 Asn^{250}, which is invariant in the SLC11 family and substituted for Thr or Ser in the outgroup. Because replacement of MntH Asn^{401} with Thr produces a phenotype similar to the exchange for the matching outgroup moiety (Gly) (10), we analyzed MntH mutants N37T, N250T, and N401T. The TM location of the targeted sites is schematized (Fig. 1*A*) based on previous predictions and experimental determinations (11, 14, 15, 39). The mutant proteins displayed membrane expression levels similar to MntH-WT, indicating that the substitutions were structurally well tolerated (Fig. 1*B*).

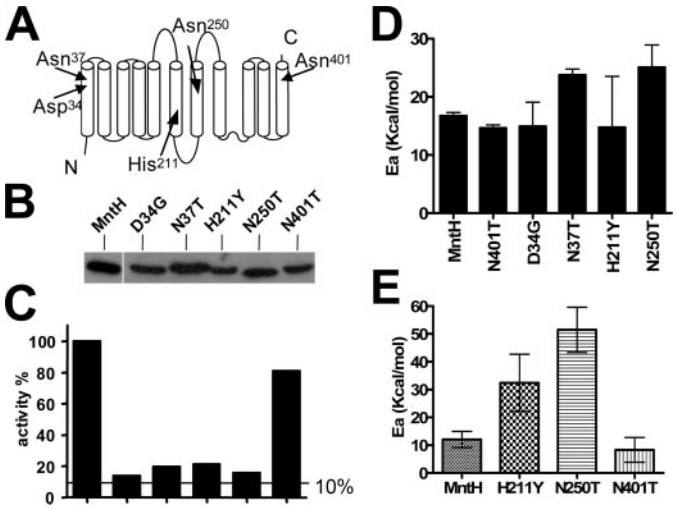

FIGURE 1. **Thermal activation of *E. coli* MntH mutants activity.** *A*, low resolution *E. coli* MntH topological model. *Arrows* indicate the predicted location of MntH residues corresponding to SLC11-specific sites. *B*, Western blot of c-Myc-tagged mutants (80 μg of membrane proteins/lane). *C*, Cd^{2+} uptake by *E. coli* GR536 cells expressing MntH-WT and -mutants at SLC11 type II evolutionary sites. Uptake of 10 μM $^{109}Cd^{2+}$ (60 mCi/μmol) was measured for 10 s at 37 °C, pH 6.5. *D* and *E*, Arrhenius E_a plots of MntH activity (15–37 °C) deduced using the equation $k = A \times \exp^{(-E_a/RT)}$, where *k* is the rate coefficient, *A* is a constant, *R* the universal gas constant and *T*, temperature in K, for Cd^{2+} uptake quantified by radio-filter assay (*D*), and Cd^{2+}-induced H^+ uptake measured by ratiometric fluorescence analysis of intracellular pH (*E*).

TABLE 1
Kinetics of MntH Cd^{2+} transport in whole cells at pH 6.5 and 7.5

Data obtained at 37 °C in 0.05 M Pipes-Mes and 10 s after addition of $^{109}Cd^{2+}$ is shown.

MntH	$K^{0.5}_{Cd}$		V_{max}	
	pH 6.5	pH 7.5	pH 6.5	pH 7.5
	μM		*nmol/min*	
Wild-type	2.6 ± 0.5	9.1 ± 2.9	13.4 ± 2.1	31.2 ± 4.6
D34G[a]	21.1 ± 3.6	32.0 ± 9	10.4 ± 0.7	8.1 ± 0.3
N37T[a]	15.0 ± 2.5	43.0 ± 15	9.7 ± 0.3	10.0 ± 3.0
H211Y[a]	4.4 ± 1.1	NA[b]	4.3 ± 0.3	NA
N250T[a]	4.3 ± 0.1	12.5 ± 0.8	3.7 ± 0.1	3.5 ± 0.4
N401T	2.1 ± 0.6	10.4 ± 0.8	7.7 ± 0.7	28.2 ± 0.9

[a] Data collected 1 min, pH 6.5, and 2 min, pH 7.5, after addition of $^{109}Cd^{2+}$.
[b] NA, not applicable (similar to Δ*mntH* cells).

Characterization of E. coli MntH Cd^{2+} and H^+ Transport in Vivo—To study the effects of the external pH on the kinetics of MntH, we measured $^{109}Cd^{2+}$ uptake and Cd^{2+}-dependent intracellular acidification in intact *E. coli* cells. Cd^{2+} uptake by MntH-WT (Fig. 1C) revealed $K^{0.5}_{Cd}$ values at 37 °C of 2.6 ± 0.5 μM at pH 6.5 and 9.1 ± 2.9 μM at pH 7.5 (data fitted to the Michaelis-Menten equation, Table 1). The maximal velocity (V_{max}) of Cd^{2+} transport was lower at pH 6.5 compared with pH 7.5. MntH-catalyzed Cd^{2+}-induced H^+ uptake was activated by increasing amounts of Cd^{2+}, with $K_{0.5}$ values at 23 °C ranging from 0.78 to 1.4 μM Cd^{2+} (pH 4.7–5.7, respectively, Table 2 and supplemental Fig. 1, *B* and *C*). In both systems, lowering the external pH increased MntH affinity for Cd^{2+}.

To discriminate carrier-type from channel-mediated transport the Arrhenius E_a values were measured (28, 40) for Cd^{2+}

TABLE 2

Kinetics of MntH Cd^{2+}-induced intracellular acidification at pH 4.7 and 5.3

Data were obtained at 23 °C in 50 mM citrate-phosphate buffer and 1000 s after addition of Cd^{2+}.

MntH	$K_{0.5}$		V_{max}	
	pH 4.7	pH 5.3	pH 4.7	pH 5.3
	μM		pM/s	
Wild-type	0.8 ± 0.2	1.4 ± 0.3	98 ± 6	34 ± 2
D34G	NA[a]	NA	NA	NA
N37T	NA	NA	NA	NA
H211Y	30 ± 9	500 ± 300	116 ± 9	28 ± 7
N250T	140 ± 10	40 ± 20	81 ± 8	18 ± 2
N401T	4 ± 1	5 ± 2	190 ± 20	101 ± 7

[a] NA, not applicable (D34G, no activity; N37T, $K_{0.5} \sim 600$ μM at pH 4.7).

uptake and Cd^{2+}-induced intracellular acidification. E_a values (Fig. 1, *D* and *E*) were in the range of those obtained for carriers (10.7–26.3 kcal/mol, *versus* channels, 4.3–8.1 kcal/mol) supporting the notion of MntH transport cycle and intramolecular structural rearrangement. This could involve for instance, an external open conformation loading Me^{2+} and H^+ to translocate them to the inner face of the membrane, before unloading and then rapidly back-translocating to reload (16).

MntH Cd^{2+} uptake activity was drastically reduced for four of the mutants studied (Fig. 1*C*). Further analyses of MntH Cd^{2+}/H^+ symport kinetics and thermodynamics revealed various types of effects (Tables 1 and 2), which can be summarized as: (i) low affinity Me^{2+} uptake and little H^+ transport (Asp^{34} and Asn^{37}), (ii) reduced Me^{2+} uptake but significant residual H^+ uptake (Asn^{250}, His^{211}), or (iii) slight opposite variations in Cd^{2+} and H^+ uptake (Asn^{401}), and (iv) impaired transporter cycling (Asn^{37}, Asn^{250}, and His^{211}). Individual phenotypes are detailed below.

MntH TMS1 Asp[34] Is Essential for Coupling H[+] and Cd[2+] Uptake—Kinetic analyses of the MntH-D34G mutant revealed dose-dependent Cd^{2+} uptake, and $K_{Cd}^{0.5}$ values that were increased about 2- and 10-fold compared with MntH-WT at pH 7.5 and 6.5, respectively, but Cd^{2+}-induced H^+ uptake was not detected even when using 1 mM Cd^{2+} (supplemental Fig. 2*D*). The unique properties of the MntH-D34G mutant, such as $K_{Cd}^{0.5}$ values little affected by the external pH and lack of H^+ transport, suggested that exchange of Asp^{34} uncoupled Cd^{2+} uptake from H^+ influx.

To determine whether a conformational rearrangement was involved we tested the E_a of Cd^{2+} uptake by MntH-D34G, which was similar to MntH-WT (Fig. 1*D*). The E_a of H^+ uptake could not be measured because no significant activity was detected for any Asp^{34} variant (supplemental Fig. 2*D*). This indicated that mutation of Asp^{34} could directly affect H^+ binding *versus* transporter cycling, which was confirmed *in vitro* by lack of a Cd^{2+}-induced MntH-dependent variation of $\Delta\psi$ in right-side out vesicles (see below "Electrogenicity of MntH-dependent Forward Cd^{2+} Transport " and Fig. 3*E*).

MntH TMS6 His[211] Role in Cd[2+] Transport is pH-dependent—The exchange of TMS6 His^{211} for Tyr had pH-dependent effects on MntH Cd^{2+} uptake. Compared with MntH-WT, the $K_{Cd}^{0.5}$ value of MntH-H211Y doubled at pH 6.5, but at pH 7.5, Cd^{2+} uptake levels were indistinguishable from cells lacking a functional MntH (Table 1). At pH 6.5, the MntH-H211Y V_{max} value was reduced (Table 1), and the E_a value possibly affected (Fig. 1*D*). Similar strongly pH-dependent Me^{2+} uptake activity has been reported for Nramp2 mutation at the homologous site, H267A, which was compensated for by lowering the external pH (41).

To examine whether this SLC11 invariant His residue is crucial for pH-dependent Me^{2+} binding we measured Cd^{2+}-induced variations in intracellular pH (Table 2, supplemental Fig. 1, *B* and *C*). The apparent $K_{0.5}$ of MntH H211Y was several 100-fold increased at pH 5.3 compared with WT. The V_{max} value for H^+ accumulation showed that this mutant still catalyzed H^+ uptake, although the E_a value of H^+ transport was elevated (Fig. 1*E*). The results thus indicated that replacement of MntH TMS6 His^{211} alters H^+ binding and the catalytic cycle of Cd^{2+} binding and transport.

MntH Asn[37], Asn[250], and Asn[401] Contribute Indirectly to Cotransport Activity—The MntH Asn^{250} mutant also showed unique effects compared with MntH-WT: up to an 100-fold increase in the apparent $K_{0.5}$ value for Cd^{2+}-induced H^+ uptake at pH 4.7 and reduced V_{max} values (Table 2 and supplemental Fig. 1, *B* and *C*); strong reduction in the V_{max} values for Cd^{2+} uptake, especially at pH 7.5 and a lesser increase of $K_{Cd}^{0.5}$ values, mainly at pH 6.5 (Table 1); and elevated E_a values of both Cd^{2+} and H^+ transport (Fig. 1, *D* and *E*). Because N250Q exchange was not conservative (compared with N401Q, supplemental Fig. 2) these results indicated a role of Asn^{250} in transporter cycling.

Although replacement of Asn^{37} affected Cd^{2+} and H^+ transport kinetics similarly to Asp^{34} mutation, maybe due to proximity of these sites, important differences were noted: the MntH-N37T mutation did not abrogate Cd^{2+}-induced H^+ uptake (supplemental Fig. 2*D*), whereas the E_a value of Cd^{2+} transport was elevated (Fig. 1*D*), and $K_{Cd}^{0.5}$ values remained pH-dependent (Table 1). The MntH Asn^{37} residue may, similarly to Asn^{250}, take part in conformational changes during the transport cycle.

MntH mutation Asn^{401} to Thr had less impact on transport kinetics than N37T and N250T exchanges (Fig. 1), consistent with Asn to Gln replacement that was conservative only at site 401 (supplemental Figs. 1 and 2). Main effects were on MntH-N401T V_{max}, which was reduced for Cd^{2+} uptake especially at pH 6.5 (Table 1), but increased ~2-fold for Cd^{2+}-induced H^+ uptake, independent of the external pH (Table 2, supplemental Fig. 1, *B* and *C*). pH-dependent variations of $K_{Cd}^{0.5}$ were not correlated with Cd^{2+} transport V_{max} values. Such effects supported previous observations linking nonconservative mutations of Asn^{401} to intracellular acidification in the absence of added Cd^{2+} (10), due to apparently opposite effects on the V_{max} values of Me^{2+} and H^+ uptake.

Characterization of MntH-catalyzed Forward Metal Uptake in Vitro—To confirm the uncoupling effect of the MntH D34G mutation observed *in vivo* we studied Cd^{2+} transport *in vitro* using RSOV. ISOV were used for comparison. MntH-dependent $^{109}Cd^{2+}$ uptake in 0 trans conditions showed different requirements for RSOV or ISOV preparations (Fig. 2, *A* and *B*). Uptake into RSOV was stimulated about 10-fold of the background levels by addition of millimolar amounts of Ca^{2+} and the respiratory substrate PMS/Asc (42), whereas 10-fold more metal was necessary to obtain about 3-fold stimulation of back-

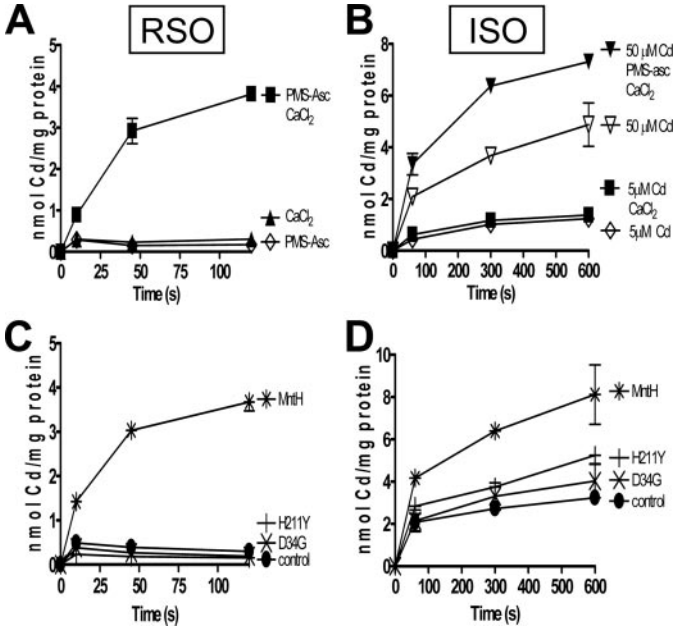

FIGURE 2. **MntH-dependent Cd^{2+} transport in vesicles of correct and inverted orientations.** Cd^{2+} uptake was measured in right-side out vesicles (RSOV, *A* and *C*) and inside out vesicles (ISOV, *B* and *D*) using, respectively, 5 or 50 μM $^{109}Cd^{2+}$ (60 mCi/μmol) in 0.1 M Pipes-Mes, pH 6.5, and PMS/Asc as respiratory substrate where indicated, in the presence or absence of 10 mM $CaCl_2$. Control values, vesicles harboring no MntH protein. *A* and *B*, transport by MntH-WT was performed as described under "Experimental Procedures"; control values were subtracted. *C* and *D*, forward and reverse Cd^{2+} transport by MntH-WT, -D34G, and -H211Y.

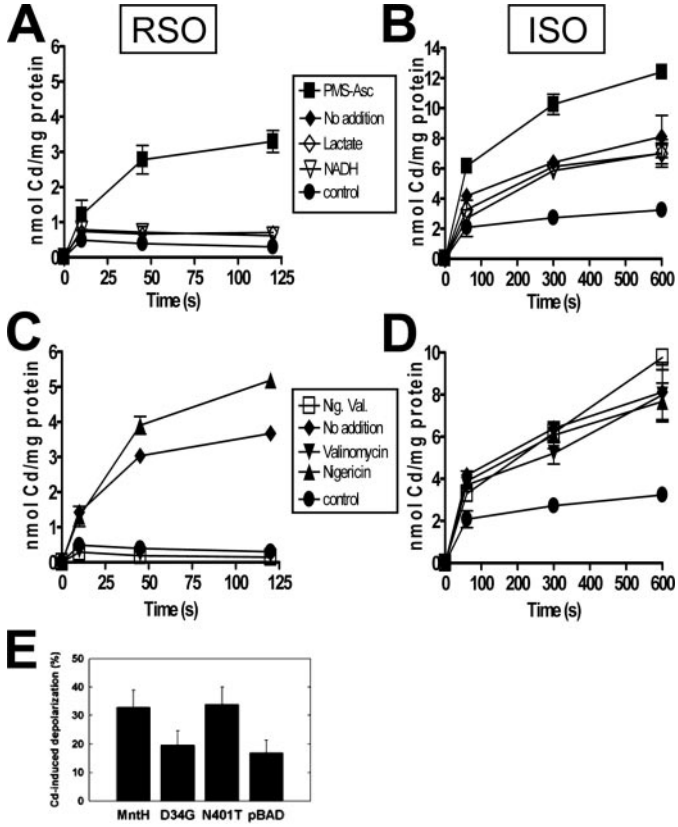

FIGURE 3. **Energy requirements and electrogenicity of MntH Cd^{2+} uptake.** Time course of transport was measured at 23 °C, pH 6.5, with 5 μM Cd^{2+} (RSOV; *A* and *C*) or 50 μM Cd^{2+} (ISOV; *B* and *D*). Vesicles were preincubated with respiratory substrates (*A* and *B*) or K^+ and/or H^+ ionophores (*C* and *D*, in presence of 0.1 M KCl) before measuring transport by radiofilter assay. *Control*, vesicles harboring no MntH protein. *E*, MntH-dependent depolarization of $\Delta\psi$ induced in RSOV by addition of Cd^{2+} and measured as described in supplemental Methods. Mean ± S.E. of 7–14 replicas; *pBAD*, vector control.

ground uptake in ISOV (Fig. 2, *A* and *B*). However, both Cd^{2+} uptake activities were saturable, temperature-dependent (data not shown), and required an active transporter: mutants at sites thought to interact directly with Cd^{2+} and H^+ showed little uptake in conditions otherwise favorable for MntH-WT (Fig. 2, *C* and *D*).

MntH uptake in RSOV was stimulated by a potent electron donor (PMS/Asc *versus* lactate or NADH, Fig. 3*A*). In the presence of 1 unit of ΔpH (10-fold variation in $[H^+]$), Cd^{2+} uptake was increased by adding the H^+/K^+ ionophore nigericin, which converts ΔpH into increased $\Delta\psi$ (43), and it was abrogated using the K^+ ionophore valinomycin, which dissipates $\Delta\psi$ (Fig. 3*C*). Without external K^+, Cd^{2+} transport still required PMS/Asc and Ca^{2+} but was not affected by nigericin, slightly stimulated with valinomycin, and the protonophore CCCP abrogated it (data not shown). Thus, MntH forward Me^{2+} uptake activity is proton-dependent.

In contrast, and contrary to the expected inhibition by $\Delta\psi$ (positive inside) of a proton-motive force-dependent mechanism of Cd^{2+} uptake, MntH-dependent activity in ISOV persisted in the presence of 10 mM D-lactate or 5 mM NADH (Fig. 3*B*) and was indifferent to nigericin, valinomycin, or both as well as up to 100 μM CCCP (Fig. 3*D*). Also, compared with RSOV, PMS/Asc and Ca^{2+} induced little stimulation of Cd^{2+} uptake in ISOV, which was nullified by CCCP (consistent with ~90% homogeneous ISOV preparations, supplemental Fig. 3*D* and data not shown). These data distinguished MntH "reverse " transport from proton-dependent forward transport activity.

Electrogenicity of MntH-dependent Forward Cd^{2+} Transport—Observation of Me^{2+} uptake driven by $\Delta\psi$ only (negative inside) into RSOV preparations (Fig. 3*C*) was consistent with *in vivo* data (supplemental Fig. 4*A*) using an *E. coli* Δ*unc* strain, unable to convert ATP and the proton-motive force, in which MntH Mn^{2+} uptake at pH 7.4 (ΔpH ~ 0) was independent of ATP and abrogated by micromolar amounts of CCCP. These data suggested that MntH forward transport activity, symporting Me^{2+} and H^+, is electrogenic, *i.e.* it produces charge imbalance across the membrane.

Consequently, MntH activity should contribute directly to modulate $\Delta\psi$; using conditions where RSOV are energized with $\Delta\psi$ only (negative inside), MntH-dependent symport of Me^{2+} and H^+ should in turn reduce $\Delta\psi$. Such MntH-dependent charge movement across the membrane was quantified by following Cd^{2+}-induced depolarization of $\Delta\psi$. Because addition of 100 μM Cd^{2+} to RSOV harboring MntH-D34G yielded low level Cd^{2+} uptake at pH 6.5 (data not shown), this concentration was used to follow the Cd^{2+}-induced variation in $\Delta\psi$ (less negative inside). Similar depolarization was observed with the MntH-WT and -N401T mutants (Fig. 3*E*), reflecting electrogenic, non-compensated charge movement across the vesicle membrane. Deficient electrogenicity of MntH-D34G supported the loss of the Cd^{2+}-induced H^+ symport in this mutant.

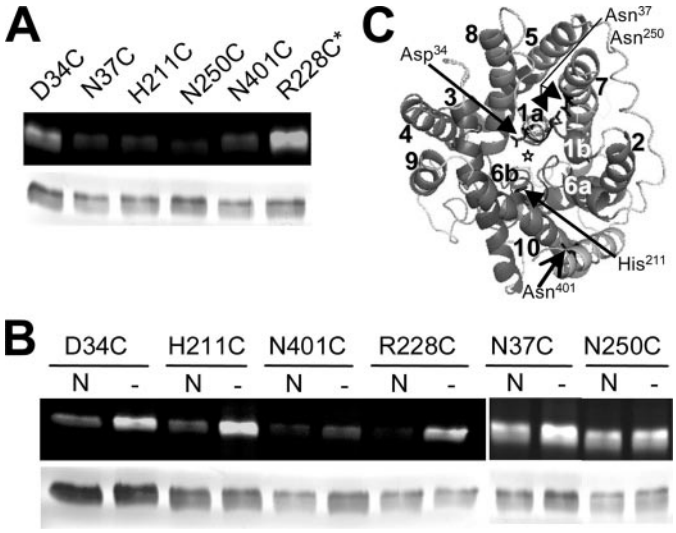

FIGURE 4. **Topological accessibility of MntH TMS1 Asp^{34} and TMS6 His^{211}.** *A* and *B*, *in situ* accessibility of single cysteine residues introduced in MntH 12TMS-His$_{10}$ at either SLC11-specific sites or the control cytoplasmic site 228 (supplemental Fig. 3) was assayed using RSOV. *Top panel*, in-gel F5M fluorescence was visualized under UV; *bottom panel*, silver nitrate staining of the corresponding Ni^{2+} affinity purified proteins. *In situ* accessibility was revealed by direct labeling with F5M (*A*; except *, labeling after solubilization), or reaction with NEM (*N*) or not (−) before solubilization and F5M labeling (*B*), as described under "Experimental Procedures." *C*, view from the periplasm of the LeuT-based SLC11 model obtained by threading. Half-helices 1a and 6b are placed at the *bottom*, orthogonal to the membrane plan; sites comprising the top "*loop EL4*" (44) are not shown for clarity. Positions predicted for cation binding sites Asp^{34} and His^{211}, close to the center (indicated by *star*), and for the other sites studied are indicated by *arrows*. *Numbers 1–5* and *6–10* designate the TMS forming the inverted domains.

MntH Asp^{34} and His^{211} Are Accessible to Solvent and Predicted to Line a Permeation Pathway—Direct involvement of Asp^{34} in coupled Cd^{2+} and H^+ uptakes suggested that this residue could interact with either cation through a water-filled "pore," and should thus be solvent-accessible. To address this possibility, single Cys mutants were produced using a MntH construct that had been modified to add a 12th TMS and a C-terminal cytoplasmic His tag that allowed affinity purification. The MntH 12TMS-His$_{10}$ construct exhibited transport activity similar to MntH-WT (supplemental Figs. 3*F* and 4*B*). RSOV harboring each of the MntH single Cys mutants at the five Nramp/SLC11-specific sites (34, 37, 211, 250, and 401) were probed *in situ* with sulfhydryl reagents, either bulky and polar, F5M, or small and permeable, NEM.

Strikingly, only two sites were reachable *in situ*: Cys^{34} was freely accessible to F5M (Fig. 4*A*) and Cys^{211} reacted solely with NEM (Fig. 4, *A* and *B*). These results seemed consistent with the Asp^{34} and His^{211} respective predicted locations in TMS1 and TMS6 and their distinct direct roles in Me^{2+}/H^+ symport. Also, TMS1 Cys^{37} and TMS7 Cys^{250} became labeled with F5M after solubilizing MntH (Fig. 4, *A* and *B*), supporting possible roles in the transporter motion. TMS11 Cys^{401} was marginally accessible (Fig. 4, *A* and *B*) implying that it participates to tight inter-helical contacts; exchanging Asn^{401} for a smaller side chain increased cation uptake, whereas a similar sized moiety limited it (*e.g.* supplemental Fig. 4*B* and 2, *A* and *C*, respectively, Cys and Gln; prior data using Gly and Thr, see Ref. 10). The results of site-directed labeling thus converged with functional data to demonstrate that SLC11-specific residues contribute critically to MntH transport by either binding substrates directly (Asp^{34}, His^{211}) or contributing to inter-helices contacts (Asn^{37}, Asn^{250}, and Asn^{401}).

Three-dimensional mapping of functional sites is crucial to understand catalytic mechanisms. We determined whether known transporter structures could help model a spatial distribution for the SLC11-specific functional sites. Several template structures, *e.g.* LeuT, glycerol-3-phosphate transporter, EmrD, and chloride channel, were frequently ranked as significant hits with most programs and for each SLC11 sequence tested. However, only the LeuT/SLC6 family structure (44) fully supported our functional and topological data (Fig. 4*C* and supplemental Fig. 5). Additional predictions obtained using Modeler and either single sequences or groups of sequences representing SLC11 phylotypes as queries produced 16 models, which were all based on the LeuT template, and with scores ranging from 0.01 to 0.76. The similarity of each of these models with the LeuT structure was quantified using DaliLite (37) yielding values in the ranges 44–60.3 (*Z*-score), 322–439 (aligned residues), 0.8–1.7 (Å, root mean square deviation), and 10–17 (% sequence identity), which indicated that SLC11 transporters may share the same general fold. The model presented (Fig. 4*C*; supplemental Fig. 5) exhibits little difference with the LeuT/SLC6 structure, with values for root mean square deviations and *Z*-score of, respectively, 1.07 Å and 7.5 (45) or 1.0 Å and 52.9 (37). This LeuT fold places both Asp^{34} and His^{211} in the inner core of the MntH molecule, as parts of extended peptides interrupting TMS1 and TMS6, and lining a water-filled pore. The three Asn^{37}, Asn^{250}, and Asn^{401} appeared directed toward inter-helix contacts and the outer fence of the model architecture (Fig. 4*C* and supplemental Fig. 5). Structural modeling of SLC11 evolutionary distinct sites thus corroborates their key functional roles.

DISCUSSION

The present study showed that MntH Asp^{34} and His^{211}, two SLC11 family-specific and ionizable residues located in TMS1 and TMS6 are necessary for binding and transport of H^+ and Me^{2+}. Whereas interdependent transport of Me^{2+} and H^+ by MntH is consistent with properties reported for eukaryotic Nramp homologs (17, 46), we demonstrated here for the first time that exchange of MntH TMS1 Asp^{34} uncoupled H^+ and Cd^{2+} transport and also reduced affinity for Cd^{2+}, but preserved pH-independent Cd^{2+} uptake and transporter cycling. Because this site was also freely accessible *in situ*, it is likely part of an H^+ translocation pathway. Exchange of MntH TMS6 His^{211} rendered affinity for Cd^{2+} more dependent on the external pH but preserved Cd^{2+}-induced H^+ transport; Cys^{211} was accessible *in situ* only to a small reagent, supporting a direct role of His^{211} (de)protonation in Cd^{2+} transporter cycling. The SLC11-specific TMS1 Asp and TMS6 His residues constitute thus functional determinants of Me^{2+} and H^+ symport.

The TMS1 Asp residue is part of a conserved DPGN motif that has been subjected to mutagenesis in studies using MntH or Nramp2 homologs, which showed loss of Me^{2+} uptake caused by Gly exchange (11, 47). The carboxyl end of Nramp2 TMS1 and adjacent extra loop were implicated in Me^{2+} binding and coupling of Me^{2+} uptake to the proton-motive force

(47). MntH scanning mutagenesis revealed that only Pro^{35} exchange did not abrogate Mn^{2+} uptake, and MntH-P35G had a marginally affected $K^{0.5}_{Mn}$ (11). Here, the role of the flanking SLC11 family-specific site Asn^{37} was detailed. Exchange of Asn^{37} seemed to perturb interactions among TMS rather than between MntH and cations, as demonstrated by inaccessibility to a small soluble compound *in situ*, impaired Cd^{2+} and H^+ transporter cycling but residual Cd^{2+}-induced H^+ transport, and pH dependence of Cd^{2+} uptake. We deduce that the SLC11 invariant tripeptide (DPG) may bear analogy to a known functional signature for $Me^{2+/+}$ transport, *i.e.* ((C/S/T)P(C/H)) that is conserved in the TMS6 of P_{1B}-type ATPases, which pump heavy metal cations using energy provided by ATP hydrolysis (48, 49). The SLC11-invariant Asp and Gly residues in TMS1 could thus contribute to Me^{2+} binding, the acidic moiety being key for H^+-coupled transport.

The His residue in TMS6 was shown previously to regulate Me^{2+} uptake via Nramp2 and MntH (10, 41). We further showed that low Me^{2+} uptake persisted with MntH-H211C (supplemental Fig. 4*B*), similar to the Nramp2 matching mutant H267C (41), and that MntH-H211Y low affinity for Cd^{2+} did not prevent H^+ uptake. It seems thus unlikely that this His residue could either bind Me^{2+} directly, or simply be part of a relay or channel enabling H^+ movement across the membrane (50, 51). Instead, (de)protonation could favor a conformation facilitating Me^{2+} translocation and transporter cycling; TonB His^{20} is an example of a TM His moiety required for transport cycling and the energy transduction event (52). The SLC11-specific TMS6 His residue is part of another conserved motif (MPH) (with exceptions in plasmodia, plants, and fungi homologs) not found in the SLC11 phylogenetic outgroup (V(P/G)Y) (10), suggesting by analogy with TMS1 that the TMS6 motif (MPH) may represent another signature for metal transport.

Strikingly, modeling SLC11 homologs on the LeuT/SLC6 structure suggests an internal symmetry (including two domains made of helices 1–5 and 6–10, similarly folded but in inverted orientation with respect to the membrane (53), and thus a possible origin for the motifs in TMS1 and TMS6, which appear central to the model transporter architecture. These two motifs in anti-parallel orientation ((DPG) and ("HPM")) form a pair of extended peptides interrupting TMS1 and TMS6. Similar pairs of discontinuous helices (α-helix-extended peptide-α-helix) constitute a salient feature in five cation transporter structures, and pairs of antiparallel discontinuous TM helices may be part of a fold shared by several cation transporter families (54).

Burying such (DPG) and (HPM) "extended peptides/polar helix termini" elements within the low-dielectric core of the membrane is not energetically favored, partly due to charges, including polar backbone groups not engaged in intra-chain hydrogen bonds. Such elements should be stabilized by interacting with adjacent residues, transported substrates (*e.g.* dehydrated cations), or by mediating alternate conformation rearrangements (44, 54). Our data indicate that interactions with Me^{2+} and/or H^+ may stabilize SLC11 TMS1 Asp and TMS6 His. Mapping to the LeuT model are other sites of potential divergence between the SLC11 family and outgroup, suggested clustering around these central motifs, (DPG) and (HPM) (supplemental Fig. 5, *C* and *D*), and possible inter-helix contacts, which could be considered in future structure/function studies using the present approach. The targeted Asn residues in TMS1, TMS7, and TMS11 affected transport without interacting with cations or being accessible to NEM *in situ* (Asn^{37}, Asn^{250}, and Asn^{401}). According to the LeuT fold, these residues may be oriented for inter-helix contacts, possibly key for transport cycling, *e.g.* TMS7 Asn^{250} and TMS1b Asn^{37}, or velocity (Asn^{401}), because TM Asn residues can drive strongly inter-helix associations (55, 56) or mediate structural motion during ion permeation (57).

Analysis of *E. coli* MntH activity *in vitro* yielded surprising results concerning activation of MntH forward Cd^{2+} transport by millimolar amounts of Ca^{2+}, and reverse Cd^{2+} transport that appeared passive. Requirement for millimolar Ca^{2+} in addition to RSOV energization was previously reported to stimulate Mn^{2+} uptake in *E. coli* RSOV (42). Because MntH is the sole manganese uptake system known in *E. coli* laboratory strains, our data may suggest a possible link between MntH transport and external Ca^{2+}, which might be reminiscent of interactions between a DMT1 mutant and Ca^{2+} (6). Strong asymmetry observed between MntH forward and reverse uptakes supports the proposition that MntH functions as a pump driven by $\Delta\psi$, accumulating cytosolic Me^{2+} against their concentration gradient. Kinetic studies of H^+-coupled transport systems have shown that $\Delta\psi$ regulates H^+ binding or uptake, and that H^+ coupling increases a transporter affinity for its substrates or provides some thermodynamic force for the translocation step (2). Such a mechanism is widespread in microbes and was conserved in higher eukaryotic systems where an acid microclimate produces a huge proton gradient (*e.g.* the epithelial brush-border membrane of the proximal intestine, site of uptake by Nramp2 of non-heme dietary iron (58), and the phagosomal lumen in phagocytes that is depleted from Me^{2+} by Nramp1 (59)). It is thus expected that future work on the *E. coli* MntH mechanism of the H^+-dependent transport will reveal additional structure-function relationships key to the Nramp/SLC11 family.

Evolutionary targeting of sites for biochemical analyses and three-dimensional validation of the results provides a framework to locate distinct TM residues key to the mechanism of the SLC11 membrane transport family. Low levels of sequence identity between SLC11 and SLC6 families (<20%) implies that the "LeuT-like" structural models obtained probably indicate a possibility that different families of cation transporters may share a general fold that could include inverted symmetry and discontinuous TM helices. SLC11 crystals will be required to ultimately validate any predicted model with resolution and accuracy. Nevertheless, the high resolution of the LeuT structure, which was corroborated by extensive biochemical and mutagenesis data, provided a high quality modeling template, and the suggested fit between the deduced architecture and SLC11 transporters topological and functional data imply that the current model holds significant potential for future studies of the SLC11 mechanism of Me^{2+}/H^+ symport and investigations of naturally occurring mutants in relation to diseases.

Acknowledgments—We thank T. A. Tompkins for providing L. casei genomic DNA (R0215), T. Pugsley for supplying E. coli strain PAP3402, J. Beaubien for technical assistance, E. Narayanan for help with ModWeb analyses, P. Gros for support, and H. R. Kaback for critical comments.

REFERENCES

1. Cellier, M., Prive, G., Belouchi, A., Kwan, T., Rodrigues, V., Chia, W., and Gros, P. (1995) *Proc. Natl. Acad. Sci. U. S. A.* **92,** 10089–10093
2. Mackenzie, B., and Hediger, M. A. (2004) *Pflugers Arch.* **447,** 571–579
3. Cellier, M. F., Courville, P., and Campion, C. (2007) *Microbes Infect.* **9,** 1662–1670
4. Fortier, A., Min-Oo, G., Forbes, J., Lam-Yuk-Tseung, S., and Gros, P. (2005) *J. Leukocyte Biol.* **77,** 868–877
5. Nevo, Y., and Nelson, N. (2006) *Biochim. Biophys. Acta* **1763,** 609–620
6. Courville, P., Chaloupka, R., and Cellier, M. F. (2006) *Biochem. Cell Biol.* **84,** 960–978
7. Cheah, J. H., Kim, S. F., Hester, L. D., Clancy, K. W., Patterson, S. E., III, Papadopoulos, V., and Snyder, S. H. (2006) *Neuron* **51,** 431–440
8. Granseth, E., Seppala, S., Rapp, M., Daley, D. O., and von Heijne, G. (2007) *Mol. Membr. Biol.* **24,** 329–332
9. Lemieux, M. J. (2007) *Mol. Membr. Biol.* **24,** 333–341
10. Chaloupka, R., Courville, P., Veyrier, F., Knudsen, B., Tompkins, T. A., and Cellier, M. F. (2005) *Biochemistry* **44,** 726–733
11. Haemig, H. A., and Brooker, R. J. (2004) *J. Membr. Biol.* **201,** 97–107
12. Makui, H., Roig, E., Cole, S. T., Helmann, J. D., Gros, P., and Cellier, M. F. (2000) *Mol. Microbiol.* **35,** 1065–1078
13. Kehres, D. G., Zaharik, M. L., Finlay, B. B., and Maguire, M. E. (2000) *Mol. Microbiol.* **36,** 1085–1100
14. Courville, P., Chaloupka, R., Veyrier, F., and Cellier, M. F. (2004) *J. Biol. Chem.* **279,** 3318–3326
15. Daley, D. O., Rapp, M., Granseth, E., Melen, K., Drew, D., and von Heijne, G. (2005) *Science* **308,** 1321–1323
16. Kaback, H. R., Dunten, R., Frillingos, S., Venkatesan, P., Kwaw, I., Zhang, W., and Ermolova, N. (2007) *Proc. Natl. Acad. Sci. U. S. A.* **104,** 491–494
17. Chen, X., Peng, J., Cohen, A., Nelson, H., Nelson, N., and Hediger, M. A. (1999) *J. Biol. Chem.* **274,** 35089–35094
18. Sacher, A., Cohen, A., and Nelson, N. (2001) *J. Exp. Biol.* **204,** 1053–1061
19. Mackenzie, B., Ujwal, M. L., Chang, M. H., Romero, M. F., and Hediger, M. A. (2006) *Pflugers Arch.* **451,** 544–558
20. Gaucher, E. A., Gu, X., Miyamoto, M. M., and Benner, S. A. (2002) *Trends Biochem. Sci.* **27,** 315–321
21. Gu, X. (2006) *Mol. Biol. Evol.* **23,** 1937–1945
22. Madabushi, S., Gross, A. K., Philippi, A., Meng, E. C., Wensel, T. G., and Lichtarge, O. (2004) *J. Biol. Chem.* **279,** 8126–8132
23. Richer, E., Courville, P., Bergevin, I., and Cellier, M. F. (2003) *J. Mol. Evol.* **57,** 363–376
24. Grass, G., Franke, S., Taudte, N., Nies, D. H., Kucharski, L. M., Maguire, M. E., and Rensing, C. (2005) *J. Bacteriol.* **187,** 1604–1611
25. Quick, M., Tomasevic, J., and Wright, E. M. (2003) *Biochemistry* **42,** 9147–9152
26. Rensing, C., Fan, B., Sharma, R., Mitra, B., and Rosen, B. P. (2000) *Proc. Natl. Acad. Sci. U. S. A.* **97,** 652–656
27. Peterson, G. L. (1977) *Anal. Biochem.* **83,** 346–356
28. Zhang, W., and Kaback, H. R. (2000) *Biochemistry* **39,** 14538–14542
29. Cheng, H. C. (2001) *J. Pharmacol. Toxicol. Methods* **46,** 61–71
30. Matsushita, K., Inoue, T., Adachi, O., and Toyama, H. (2005) *J. Bacteriol.* **187,** 4346–4352
31. Laemmli, U. K. (1970) *Nature* **227,** 680–685
32. Blum, H., Beier, H., and Gross, H. J. (1987) *Electrophoresis* **8,** 93–99
33. Pieper, U., Eswar, N., Davis, F. P., Braberg, H., Madhusudhan, M. S., Rossi, A., Marti-Renom, M., Karchin, R., Webb, B. M., Eramian, D., Shen, M. Y., Kelly, L., Melo, F., and Sali, A. (2006) *Nucleic Acids Res.* **34,** D291–D295
34. Jones, D. T., Bryson, K., Coleman, A., McGuffin, L. J., Sadowski, M. I., Sodhi, J. S., and Ward, J. J. (2005) *Proteins* **61,** Suppl. 7, 143–151
35. Wu, S., and Zhang, Y. (2007) *Nucleic Acids Res.* **35,** 3375–3382
36. Shindyalov, I. N., and Bourne, P. E. (1998) *Protein Eng.* **11,** 739–747
37. Holm, L., and Park, J. (2000) *Bioinformatics* **16,** 566–567
38. Kawabata, T. (2003) *Nucleic Acids Res.* **31,** 3367–3369
39. Rahman, M., Ismat, F., McPherson, M. J., and Baldwin, S. A. (2007) *Mol. Membr. Biol.* **24,** 407–418
40. Liu, G., Hinch, B., Davatol-Hag, H., Lu, Y., Powers, M., and Beavis, A. D. (1996) *J. Biol. Chem.* **271,** 19717–19723
41. Lam-Yuk-Tseung, S., Govoni, G., Forbes, J., and Gros, P. (2003) *Blood* **101,** 3699–3707
42. Bhattacharyya, P. (1970) *J. Bacteriol.* **104,** 1307–1311
43. Robertson, D. E., Kaczorowski, G. J., Garcia, M. L., and Kaback, H. R. (1980) *Biochemistry* **19,** 5692–5702
44. Singh, S. K., Yamashita, A., and Gouaux, E. (2007) *Nature* **448,** 952–956
45. Bowie, J. U., Luthy, R., and Eisenberg, D. (1991) *Science* **253,** 164–170
46. Gunshin, H., Mackenzie, B., Berger, U. V., Gunshin, Y., Romero, M. F., Boron, W. F., Nussberger, S., Gollan, J. L., and Hediger, M. A. (1997) *Nature* **388,** 482–488
47. Cohen, A., Nevo, Y., and Nelson, N. (2003) *Proc. Natl. Acad. Sci. U. S. A.* **100,** 10694–10699
48. Arguello, J. M. (2003) *J. Membr. Biol.* **195,** 93–108
49. Dutta, S. J., Liu, J., Stemmler, A. J., and Mitra, B. (2007) *Biochemistry* **46,** 3692–3703
50. Su, C. C., Li, M., Gu, R., Takatsuka, Y., McDermott, G., Nikaido, H., and Yu, E. W. (2006) *J. Bacteriol.* **188,** 7290–7296
51. Hu, J., Fu, R., Nishimura, K., Zhang, L., Zhou, H. X., Busath, D. D., Vijayvergiya, V., and Cross, T. A. (2006) *Proc. Natl. Acad. Sci. U. S. A.* **103,** 6865–6870
52. Larsen, R. A., Deckert, G. E., Kastead, K. A., Devanathan, S., Keller, K. L., and Postle, K. (2007) *J. Bacteriol.* **189,** 2825–2833
53. Pornillos, O., and Chang, G. (2006) *FEBS Lett.* **580,** 358–362
54. Screpanti, E., and Hunte, C. (2007) *J. Struct. Biol.* **159,** 261–267
55. Zhou, F. X., Cocco, M. J., Russ, W. P., Brunger, A. T., and Engelman, D. M. (2000) *Nat. Struct. Biol.* **7,** 154–160
56. Likitvivatanavong, S., Katzenmeier, G., and Angsuthanasombat, C. (2006) *Arch. Biochem. Biophys.* **445,** 46–55
57. Liu, K., Kozono, D., Kato, Y., Agre, P., Hazama, A., and Yasui, M. (2005) *Proc. Natl. Acad. Sci. U. S. A.* **102,** 2192–2197
58. Thwaites, D. T., and Anderson, C. M. (2007) *Exp. Physiol.* **92,** 603–619
59. Martin-Orozco, N., Touret, N., Zaharik, M. L., Park, E., Kopelman, R., Miller, S., Finlay, B. B., Gros, P., and Grinstein, S. (2006) *Mol. Biol. Cell* **17,** 498–510
60. DeLano, W. L. (2005) *Drug Discov. Today* **10,** 213–217

SUPPLEMENTARY DATA

This file contains Sup_Fig. legends 1-5, Sup_Methods1-2, Sup_Table 1, and Sup_Figs 1-5.

Sup_Fig. 1. Kinetics of MntH-dependent transport. **A**) Inhibitory effect of Mn^{2+} on MntH-dependent Cd^{2+} transport. Transport of 2.5µM Cd^{2+} ($^{109}Cd^{2+}$, 60 mCi/µmol) was measured using *E. coli* GR536 cells expressing MntH-WT at pH 6.5 and 37ºC by a quick filtration assay as described in Methods. Initial rates of transport were determined after 10 s and corrected for unspecific Cd^{2+} uptake as determined in the presence of 10 µM CCCP. Data were fitted to the Cheng-Prusoff equation (Ki= IC50 /[1+(S/K_M)] using S~K_M=2.5µM of Cd^{2+}). **B** and **C**) Determinations of $K_{0.5}$ and V_{max} of MntH-dependent Cd^{2+}-induced H^+ transport. Kinetics were deduced by fitting to the Michaelis-Menten equation of intracellular pH fluorescent measurements monitored after 1000 s (1). Cells harvested after induction of protein expression were washed and resuspended in citrate-phosphate buffer (pH 4.7-5.7) at an OD_{600} of 0.2 before addition of Cd^{2+}.

Sup_Fig. 2. Functional expression of MntH variants at Nramp family conserved sites. **A**) Western blot of c-Myc tagged membrane proteins. **B**) Disk assay of metal sensitivity of WT and mutant MntH (with or without c-myc tag, top and bottom, respectively). **C**) Disk-assay of growth at 42°C of the metallo-dependent *E. coli* Ts strain SL93 *mntH* (2) expressing WT or mutant MntH in the absence (-, no growth; +, clear lawn; +++, dense lawn) and the presence of $FeSO_4$ (diameter (mm) of growth ring around a disk impregnated with 1M salts). MntH-specific data were obtained by subtracting values observed with *mntH* cells containing pBAD as negative control. n.a., not applicable. **D**). Intracellular acidification of *mntH E. coli* cells expressing plasmid encoded MntH-WT or –mutants, and a recombinant pH-dependent ratiometric GFP, was induced by addition of 100µM Cd^{2+} and measured at 520 nm using a dual excitation at 410 and 470 nm as described in Methods.

Sup_Fig. 3. Sidedness of membrane vesicles. **A-D)** Effect of the proton-motive force (pmf) generated by respiration**.** Relative fluorescence (%) was measured using the following membrane potential probes: **A**) disC3(5) (1µM, *negative inside*) with RSOV, **B**) diBA (1µM, *positive inside*) with ISOV, and the pH probe 9-AA (9-aminoacridine; 5µM, *acid inside*) with ISOV (**C**). Arrows indicate injections of 10mM of the respiratory substrate D-lactate (Lac) as well as K^+ ionophores, 0.1µM nigericin (Nig, K+/H+ exchange) and/or 0.1µM valinomycin (Val, K+ ionophore). **D**) The extent of contamination of vesicle preparations by vesicle of opposite orientation was evaluated by measuring diS-C_3(5) response to ISOV energization, and changes in diBA-C_4(5) fluorescence after the energization of RSOV. Cross-contamination of ISOV (9

± 5%) was deduced from detection of D-lactate-induced *negative inside* membrane potential. **EF)** Topological orientation of MntH. **E**) Accessibility of selected residues previously located in extra membranous regions (predicted loops between TMS6/7 and TMS11/12; 3) was established by F5M labeling either after (+) or prior to (-) incubation with a charged and large competitor reagent (4-Acetomido-4'maleimidylstilbene-2,2'disulfonic acid, disodium salt (AmDis, 0.5mM), using the single Cys MntH mutants R228C (cytoplasmic) and G418C (periplasmic) and RSOV (left panel; top, protein silver staining) or ISOV (right panel; top, protein Coomassie staining) preparations. **F**) Metal-dependent H^+ transport by intact *E. coli* DH11S *mntH* (pGBM6-pH) cells (3) expressing MntH-WT or C-terminally 12TMS-His_{10} tagged versions of MntH-WT, -R228C and –G418C proteins was measured by dual excitation of intracellular pH-luorin as described in Methods.

Sup_Fig. 4. Metal uptake by whole cells expressing WT and mutant MntH. **A**) Influence of $\Delta\psi$ on MntH-WT activity in intact cells. An *E. coli mntH* mutant lacking the F_1F_o ATPase, strain PAP3402 [HN594 (*malTc* Δ*unc* ilv::Tn10 *arg his*; 4) carrying an F' lacIq pro] Δ*mntH* (pBAD-MntH) was used to measure Mn^{2+} uptake in absence of ΔpH (pH_{out} ~pH_{in} ~7.4). Uptake of 3 μM Mn^{2+} ($^{54}Mn^{2+}$, 41 μCi $mmol^{-1}$) was measured for 6 min at 37ºC, by a quick filtration assay. Cells were pre-incubated for 3min with metabolic inhibitors, either μM amount of membrane protonophore (CCCP), to collapse $\Delta\psi$, or mM amount of arsenate, which depeletes ATP stores, measured using a Luciferase ATP Determination kit (Sigma). Data represent the mean of at least 2 independent experiments; bars represent SE. **B**) Disk-assays of bacterial growth during expression of MntH-WT and MntH variants (12TMS-His_{10} constructs) in the presence of indicated metals. Cells in exponentially growth phase were plated on top agar and incubated at 37ºC for 16h after adding disks impregnated with metal solutions. Mean diameter of cell growth inhibition ± SE are presented (control values obtained with cells harbouring pBAD vector alone were subtracted).

Sup_Fig. 5. LeuT-based SLC11 structural model. Views from the periplasm (**A**,**C**) and the membrane plane (**B**,**D,E**) of a complete representative SLC11 model (**A**,**B,** ModBase entry Q9RPF2 [MNTH2_PSEAE]), a selection of sites representing candidate type II evolutionary rate-shifts (**C**,**D**, corresponding to residues that are conserved in the SLC11 family and matched by different residues, also conserved in the outgroup), or its superimposition on the SLC6/LeuT template structure (**E**; 5). The color code used to identify the TMS (**A-D**) is indicated (Box) and their inverted symmetric disposition outlined (**A**). The SLC11-specific anti-parallel motifs [D P G] (including Asp^{34} in red) and ['H P M'] (including His^{211} in blue) form "extended peptide/TM helix1b" and "TM helix6a/extended peptide" boundaries. The SLC11-specific Asn residues in TMS 1, 7 and 11 ($Asn^{37, 250, 401}$) are shown in green (**C**,**D**). Viewed from the periplasm the cations binding sites (Asp^{34} and His^{211}) appear central and close to each other, lining a water-

accessible cavity (**A**, **C**), and buried at similar depth within the hydrophobic core in views from the membrane plane (**B**,**D**).

Sup_Meth. 1. MntH solubilization and purification**.** RSOV or ISOV containing given MntH 12TMS-His_{10} constructs served as starting material for solubilisation and purification. Membrane vesicles were solubilized at a protein concentration of 5mg/mL in 0.1M Pipes-MES, pH 7.5/20% glycerol/1M NaCl (P buffer) with 2% (w/v) n-dodecyl β-D-maltoside (DDM) for 1 hour at 4°C or 0.8 % (w/v) cetyltrimethyl-ammoniumbromide (CTAB) for 30min at 30°C. The soluble fraction was collected as the supernatant after ultracentrifugation (106,000 x g; 1hour) and incubated for 3 hr at 4°C in presence of Ni-sepharose (GE Healthcare, Baie d'Urfé, Qc) and 20mM imidazole. Batch purification was performed with three sequential 1mL washes in P buffer containing 20, 40 and 100 mM imidazole, respectively. Elution was performed using 40µL of P buffer containing 250mM imidazole.

Sup_Meth. 2. Electrogenicity of MntH forward transport in vitro. Fluorescent data acquisition began following addition to MntH-WT RSOV incubated in 0.1 M Pipes/Mes pH 7.5, 0.1 M KCl and 10 mM $CaCl_2$, of (see below, 1) the Δψ sensitive fluorescent probe diSC3, (2) asc, (3) PMS, and (4) nigericin, which yielded the baseline level of fluorescence intensity corresponding to $\Delta\psi_{max}$ *(a)*, before adding (5) 100 µM Cd^{2+}, which resulted in a variation of the fluorescence level detected depending on MntH activity induced by Cd^{2+} addition (*b*), and (6) valinomycin, which collapsed Δψ (*c*). Electrogenicity of Cd^{2+} transport was deduced form the mean of the ratio (c-a/b-a).

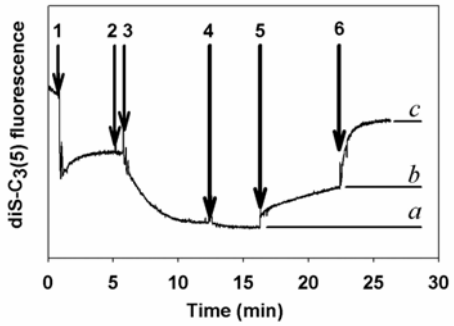

Supplementary Table

Sup_Table I. Sequence of the oligonucleotide primers used in this study

Primer	Sequence[a]
Wild type	A I G Y I D P G N F A
	5' G GCG ATT GGT TAT ATC GAT CCC GGT AAC TTT GCG
D34E	5' G GCC ATT GGT TAT ATC *GAG* CCC GGT AAC TTT GC
D34C	5' G GCC ATT GGT TAT ATC *TGT* CCC GGT AAC TTT GC
Wild type	G Y I D P G N F A T N I Q
	5' GGT TAT ATC GAT CCC GGT AAC TTT GCG ACC AAT ATT CAG GC
N37Q	5' C GAT CCC GGT *CAG* TTT GCG ACC A
N37C	5' GGT TAT ATC GAT CCC GGT *TGC* TTT GCG ACC AAT ATT CAG GC
Wild type	A T I M P H V I Y L H S S
	5' GCG ACG ATT ATG CCG CAT GTG ATT TAT TTG CAC TCC TCG C
H211C	5' GCG ACG ATT ATG CCG *TGT* GTG ATT TAT TTG CAC TCC TCG C
Wild type	T I A G F V N L A M M A
	5' G ACT ATT GCC GGT TTT GTC AAT CTG GCG ATG ATG GCT AC A
N250T	5' G ACT ATT GCC GGT TTT GTC *ACA* CTG GCG ATG ATG GCT AC
N250Q	5' CT ATT GCC GGT TTT GTC *CAG* CTG GCG ATG ATG GCT
N250C	5' ACT ATT GCC GGT TTT GTC *TGT* CTG GCG ATG ATG GCT AC A
Wild type	V L V V A L N I W L L V G
	5'GTG CTG GTC GTG GCG CTG AAT ATC TGG TTG TTG GTG GGG
N401Q	5' G GTC GTG GCG CTG *CAG* ATC TGG TTG TTG GTG GGG
N401C	5'GTG CTG GTC GTG GCG CTG *TGT* ATC TGG TTG TTG GTG
Wild type	P T S I A G F F G D H
	5' G CCA ACT AGT ATC GCC GGA TTC TTC GGC GAT CAT C
G418C	5' G CCA ACT AGT ATC GCC *TGC* TTC TTC GGC GAT CAT C
R228C	Appeared fortuitously, codon change CGT to *TGT*
MntH *StuI* 3'	5' AAC TAC AGG CCT AAC GCC GTC CCC ACC
Casei TM5'	5' CCT TAA AGG CCT GCC AAC TAG TAT CGC CGG ATT
Casei TM 3'	5' TCG TCT AGA TAG ATC TTG CTT TCG CCT CTT T
12 TMS-His_{10}	5' GAC TCT AGA TGT GAT GGT GAT GGT GAT GGT GAT GGT GAT GAG ATC TTG CTT TCG CCT CTT TTT C

[a] sequence of site directed mutated codons is indicated in bold
Restriction sites are underlined

References

1. Chaloupka, R., Courville, P., Veyrier, F., Knudsen, B., Tompkins, T. A., and Cellier, M. F. (2005) *Biochemistry* **44,** 726-733

2. Makui, H., Roig, E., Cole, S. T., Helmann, J. D., Gros, P., and Cellier, M. F. (2000) *Mol.Microbiol.* **35,** 1065-1078

3. Courville, P., Chaloupka, R., Veyrier, F., and Cellier, M. F. (2004) *J.Biol.Chem.* **279,** 3318-3326

4. Davidson, A. L., and Nikaido, H. (1990) *J. Biol. Chem*. **265**, 4254-4260

5. Kawabata T. (2003) Nucleic Acids Res. **31**, 3367-3369

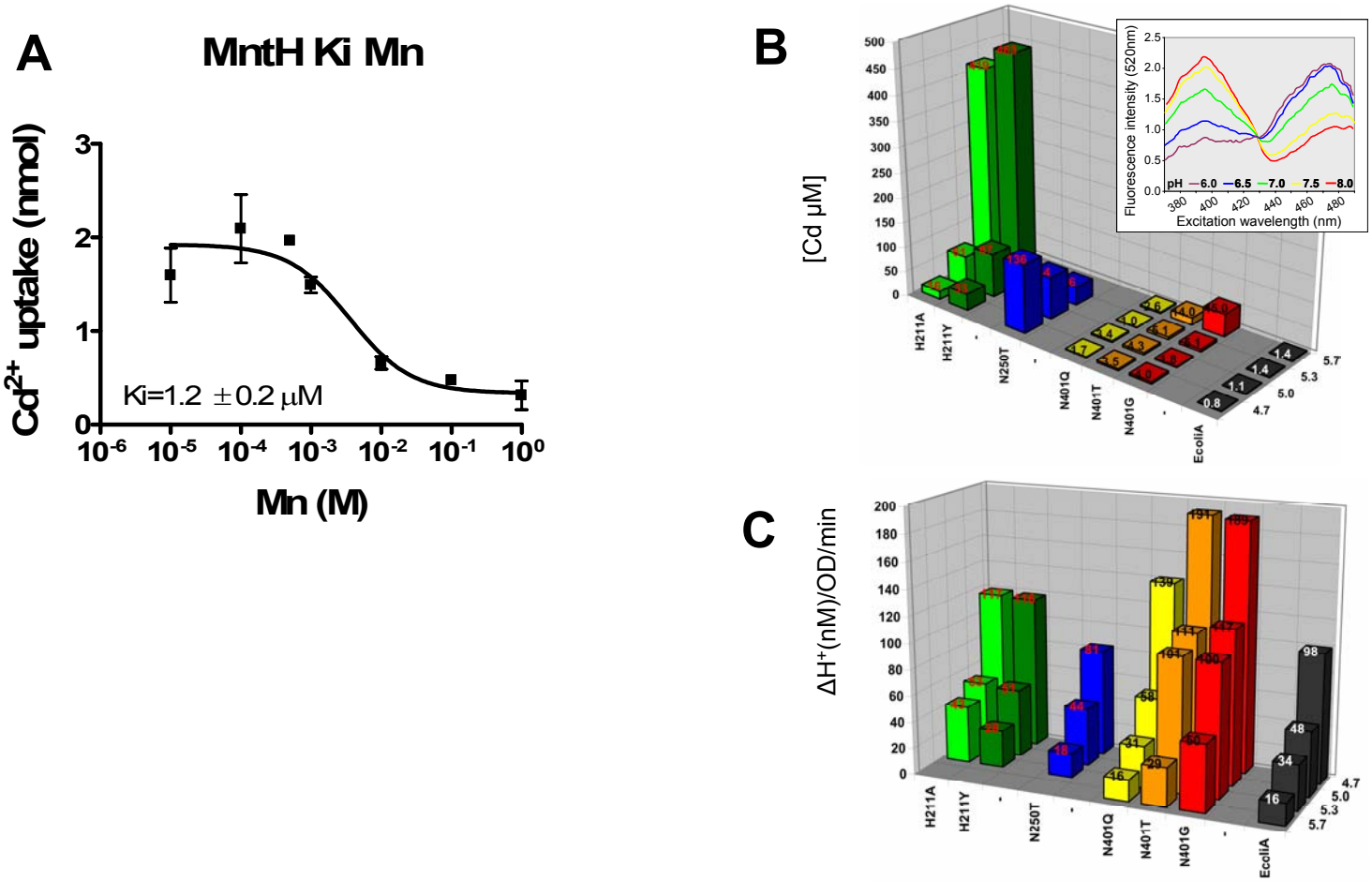

Supplementary Figure 1
Courville *et al*.

A

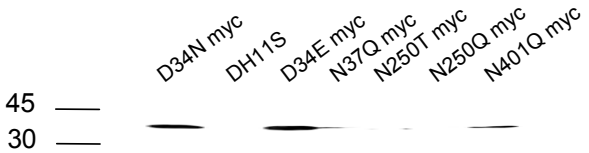

B

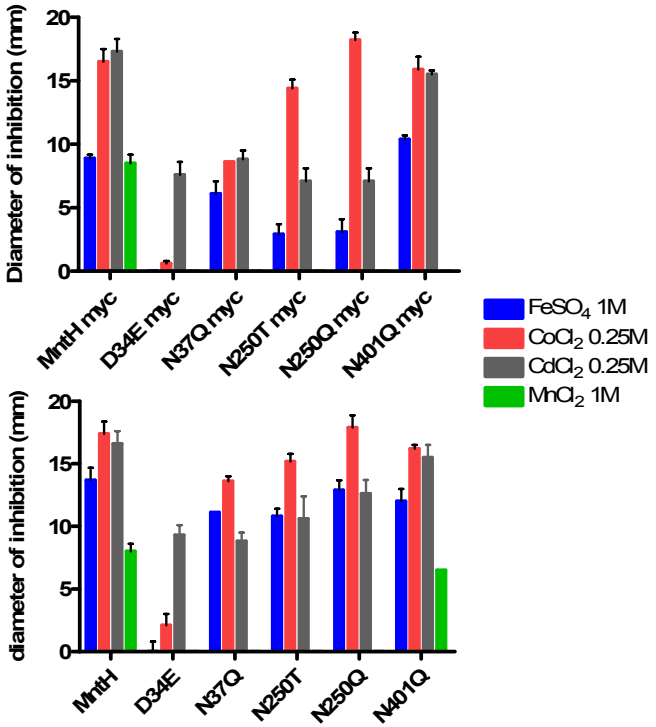

C

	+++	-	-	-	-	+
+ Fe^{2+}	n.a.	0	0	9	9	n.a.

D

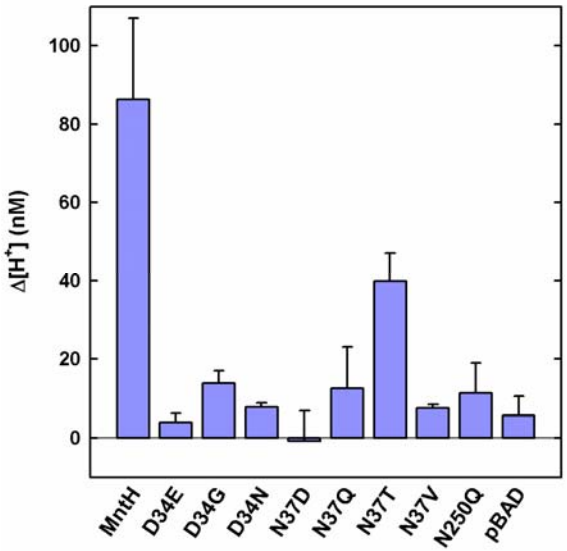

Supplementary Figure 2
Courville *et al*.

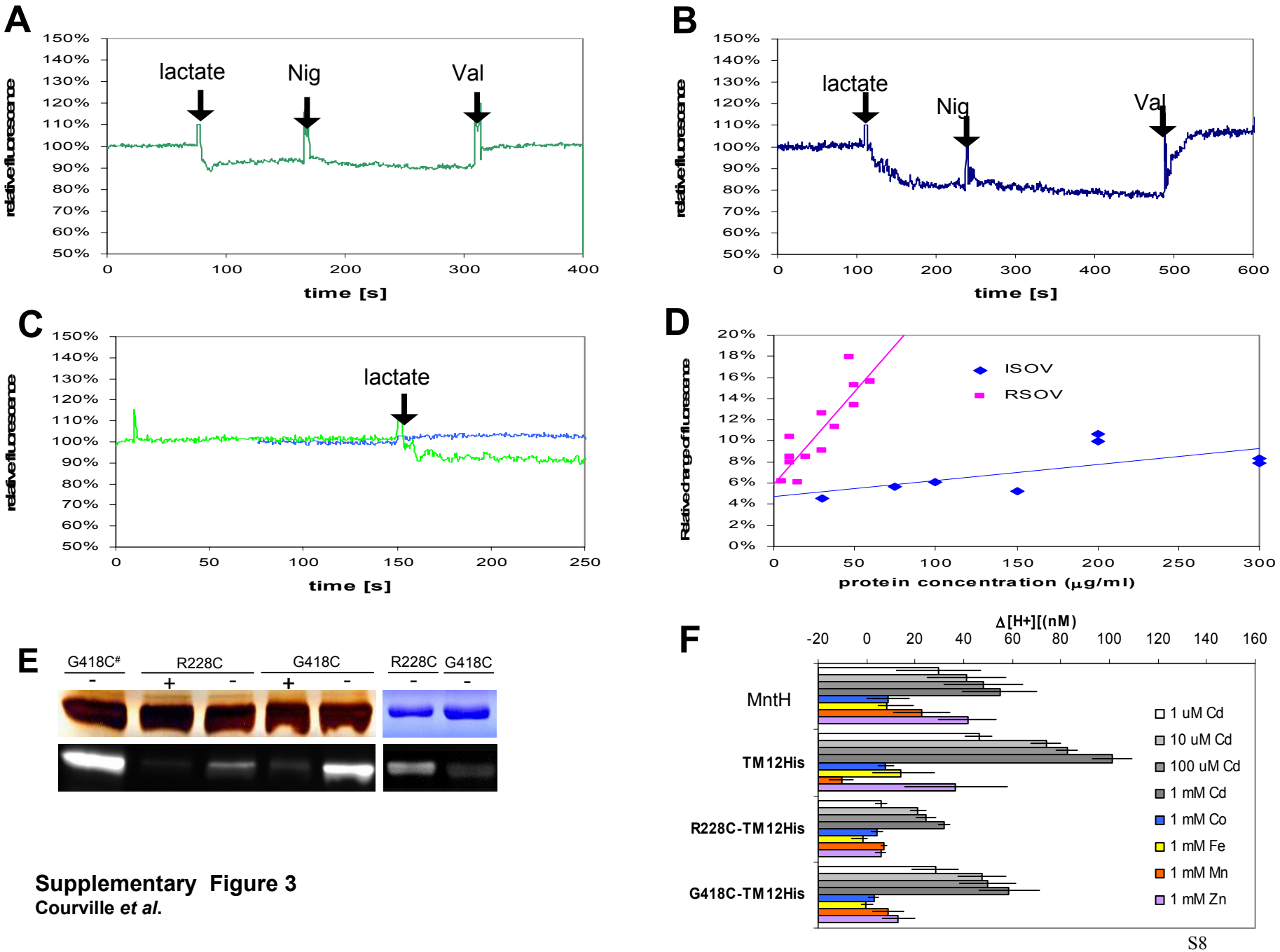

Supplementary Figure 3
Courville *et al*.

A

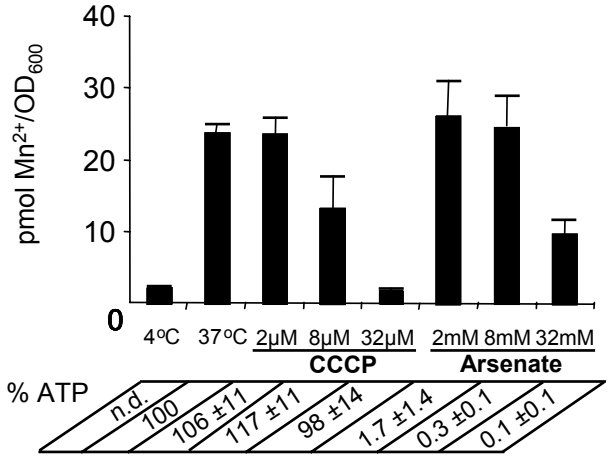

B

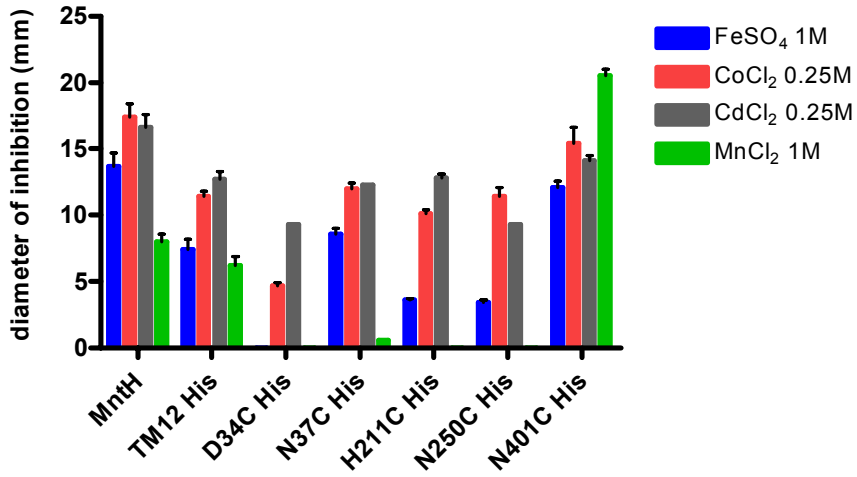

Supplementary Figure 4
Courville *et al*.

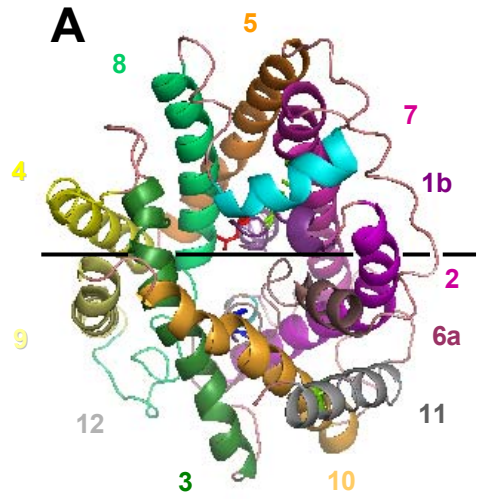

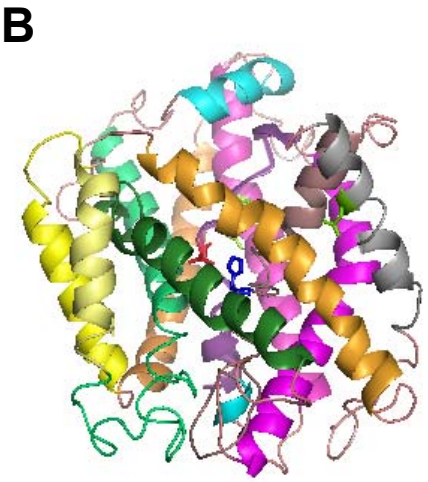

Color codes

TMS		Residues	
Purple,	1 and 6	Red,	Asp, Asp-Pro-Gly
Magenta,	2 and 7	Blue,	His, 'His-Pro-Met'
Green,	3 and 8	Green,	Asn
Yellow,	4 and 9		
Orange,	5 and 10		
Greys,	11 and 12		

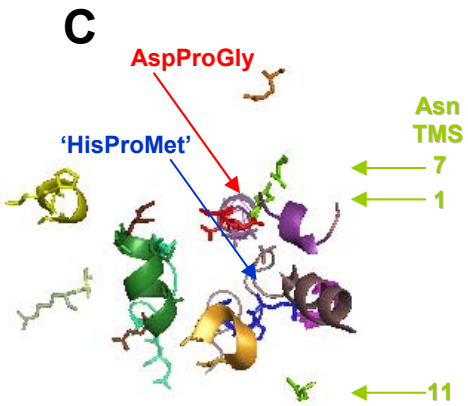

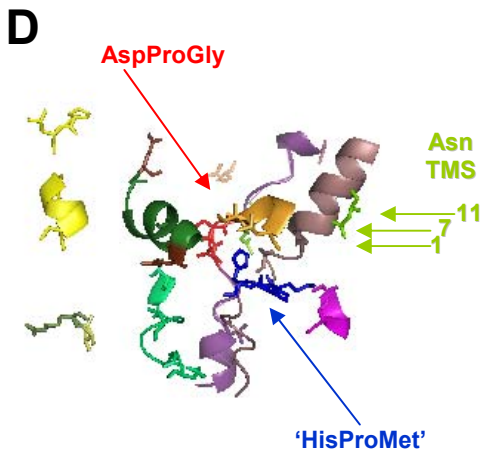

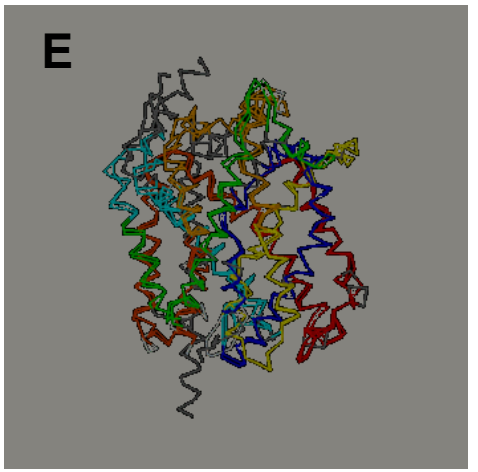

Supplementary Figure 5
Courville *et al*.

Solute Carrier 11 Cation Symport Requires Distinct Residues in Transmembrane Helices 1 and 6

Pascal Courville, Eva Urbankova, Christopher Rensing, Roman Chaloupka, Matthias Quick and Mathieu F. M. Cellier

J. Biol. Chem. 2008, 283:9651-9658.
doi: 10.1074/jbc.M709906200 originally published online January 28, 2008
